



Single-crystal elastic constants of natural ettringite

Sergio Speziale^{a,*}, Fuming Jiang^b, Zhu Mao^b, Paulo J.M. Monteiro^c, Hans-Rudolf Wenk^d, Thomas S. Duffy^b, Frank R. Schilling^e

^a *GeoForschungsZentrum Potsdam, Section 4.1, Telegrafenberg, 14473 Potsdam, Germany*

^b *Department of Geosciences, Princeton University, Princeton, NJ 08544-1003, USA*

^c *Department of Civil and Environmental Engineering, University of California, Berkeley, CA, 94720, USA*

^d *Department of Earth and Planetary Science, University of California, Berkeley, CA 94720-4767, USA*

^e *GeoForschungsZentrum Potsdam, Section 5.1, Telegrafenberg, 14473 Potsdam, Germany*

ARTICLE INFO

Article history:

Received 9 January 2007

Accepted 21 February 2008

Keywords:

Elastic moduli
Brillouin spectroscopy
Crystal structure
Sulfate

ABSTRACT

The single-crystal elastic constants of natural ettringite were determined by Brillouin spectroscopy at ambient conditions. The six non-zero elastic constants of this trigonal mineral are: $C_{11}=35.1\pm 0.1$ GPa, $C_{12}=21.9\pm 0.1$ GPa, $C_{13}=20.0\pm 0.5$ GPa, $C_{14}=0.6\pm 0.2$ GPa, $C_{33}=55\pm 1$ GPa, $C_{44}=11.0\pm 0.2$ GPa. The Hill average of the aggregate bulk, shear modulus and the polycrystal Young's modulus and Poisson's ratio are 27.3 ± 0.9 GPa, 9.5 ± 0.8 GPa, 25 ± 2 GPa and 0.34 ± 0.02 respectively. The longitudinal and shear elastic anisotropy are $C_{33}/C_{11}=0.64\pm 0.01$ and $C_{66}/C_{44}=0.60\pm 0.01$. The elastic anisotropy in ettringite is connected to its crystallographic structure. Stiff chains of $[\text{Al}(\text{OH})_6]^{3-}$ octahedra alternating with triplets of Ca^{2+} in eight-fold coordination run parallel to the *c*-axis leading to higher stiffness along this direction. The determination of the elastic stiffness tensor can help in the prediction of the early age properties of cement paste when ettringite crystals precipitate and in the modeling of both internal and external sulfate attack when secondary ettringite formation leads to expansion of concrete.

© 2008 Elsevier Ltd. All rights reserved.

1. Introduction

The understanding of the mechanical properties of cement paste and of hardened concrete is a longstanding problem of materials science and engineering. Our knowledge of the single-crystal elastic properties of the crystalline constituents of concrete is limited to very few experimental data for calcium sulfate [1] and for calcium hydroxide [2]. This makes it difficult to develop quantitative models able to predict the behavior and properties of such a complex multi-components system [3]. It is especially difficult to find in the literature data on the full elastic tensor of many of the main phases of cement paste. Traditional single-crystal techniques, based on ultrasonic interferometry and spectroscopy, are of limited help because it is difficult to obtain large fracture-free single crystals of such phases of the sizes required to perform measurements with these techniques. Brillouin spectroscopy represents an alternative and more convenient technique for the measurement of acoustic velocity in small crystalline specimens. This technique has been successfully used to determine the elastic constants of $\text{Ca}(\text{OH})_2$ [2], and we have used it to determine, in this study, the complete elastic tensor of ettringite $\text{Ca}_6\text{Al}_2(\text{SO}_4)_3(\text{OH})_{12}\cdot 26\text{H}_2\text{O}$. Ettringite is a natural trigonal sulfate and corresponds to one of the most relevant hydration products of portland cement. It is both a primary crystalline product during cement paste consolida-

tion and a secondary phase which crystallizes in hardened concrete and it plays an important role in concrete deterioration in humid environments. In addition, ettringite, effectively absorbs in its structure poisonous oxoanions from alkaline solutions produced by drainage of mining and industrial by-products, and from leachate from cement-based waste matrices with serious implications in terms of environmental impact [4–7].

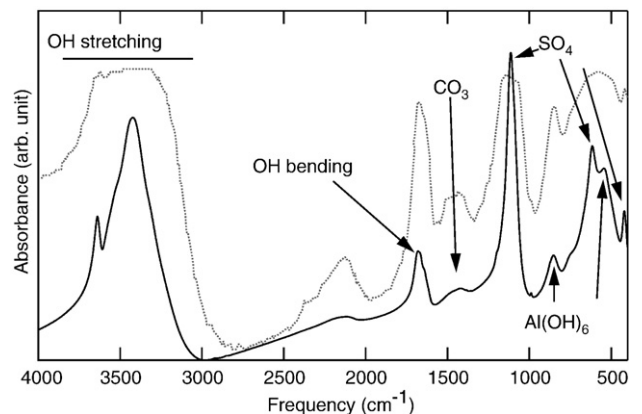


Fig. 1. Infrared absorption spectrum of ettringite. Continuous line: this study. Dotted line: from [10] converted in absorbance and rescaled for comparison.

* Corresponding author.

E-mail address: speziale@gfz-potsdam.de (S. Speziale).

Table 1
Unit-cell parameters, volume and density of ettringite

Study	a_0	c_0	V_0	ρ_0
(Ref.)	(Å)	(Å)	(Å ³)	(g/cm ³)
This study	11.240±0.001	21.468±0.006	2348.8±0.8	1.78±0.1
[20]	11.26	21.48	2358.53	1.76
[21]	11.224	21.408	2335.62	1.785
[22]	11.167±0.005	21.360±0.001	2306.81	1.9
[11]	11.229±0.001	21.478±0.003	2345.46±0.06	1.772
[23]	11.16688±0.00008	21.3537±0.0002	2306.4	1.9

[20]: Moore and Taylor (1970); [21]: ICDD file 41-1451 (1989); [22]: Berliner (1998); [11]: Goetz-Neunhoeffer and Neubauer (2005); [23]: Hartman and Berliner (2006).

In this study we determine the complete elastic tensor of ettringite and we highlight the relationship between crystal structure and elastic anisotropy in comparison with Ca(OH)₂. A detailed knowledge of the elastic properties of the single components will advance our ability to effectively model the aggregate mechanical properties of portland cement.

2. Experimental methods

The samples investigated in this study are fragments of a 10 cm×5 cm specimen of hydrothermal ettringite from N'Chwaning Mine in the giant Kalahari manganese field, South Africa [8]. While ettringite is often microcrystalline, the specimen used in this study consists of few large prismatic, colorless, transparent crystals of sizes between 2 and 8 cm and with similar orientation. In the large specimen ettringite crystals are associated with minor sulfur and opaque grains.

Ettringite forms a partial solid solution with thaumasite [Ca₃Si(OH)₆(CO₃)(SO₄)·12H₂O] [9]. We have characterized the composition

of the sample by energy dispersive X-ray analysis (EDX) of Ca, Si, Al and S (performed with a Zeiss DSM 962 scanning electron microscope equipped with a Voyager 2.6 system for EDX) and by infrared absorption spectroscopy (performed with a FTIR IR spectrometer Bruker IFS-66 with a maximum resolution of 0.25 cm⁻¹). We did not detect the presence of Si within EDX analytical resolution (0.5 wt.%). Infrared absorption measurements did not detect the typical infrared absorption bands for [Si(OH)₆]²⁻ in the 670 and 750 cm⁻¹ regions. In addition, the low intensity of the absorption band of [CO₃]²⁻ at 1400 cm⁻¹ compared with existing data for the ettringite endmember [10] confirms that our sample correspond to almost pure ettringite (Fig. 1).

The ettringite sample was also characterized by powder X-ray diffraction. Whole-spectrum Rietveld refinement yields unit-cell parameters: $a_0=11.240\pm0.001$ Å, $c_0=21.468\pm0.006$ Å, in good agreement with the extant values from the literature [11]. The calculated density is 1.78 ± 0.01 g/cm³, assuming a stoichiometric formula [Ca₆Al₂(SO₄)₃(OH)₁₂·26H₂O]. Unit-cell parameters, unit-cell volume and density are reported in Table 1.

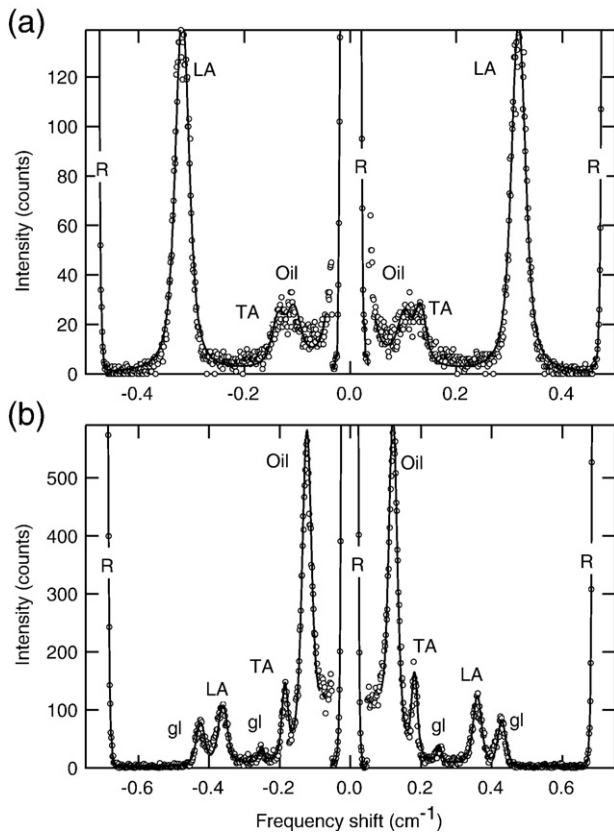


Fig. 2. Brillouin spectra collected from the two sample platelets. (a) basal plane (-0.1 0.14 - 0.04 1.91). (b) plane (1 -0.15 -0.85 -0.57). LA: sample quasi-longitudinal acoustic mode. TA: sample quasi-transverse acoustic mode. R: elastically scattered light. Oil: mineral oil. gl: glass.

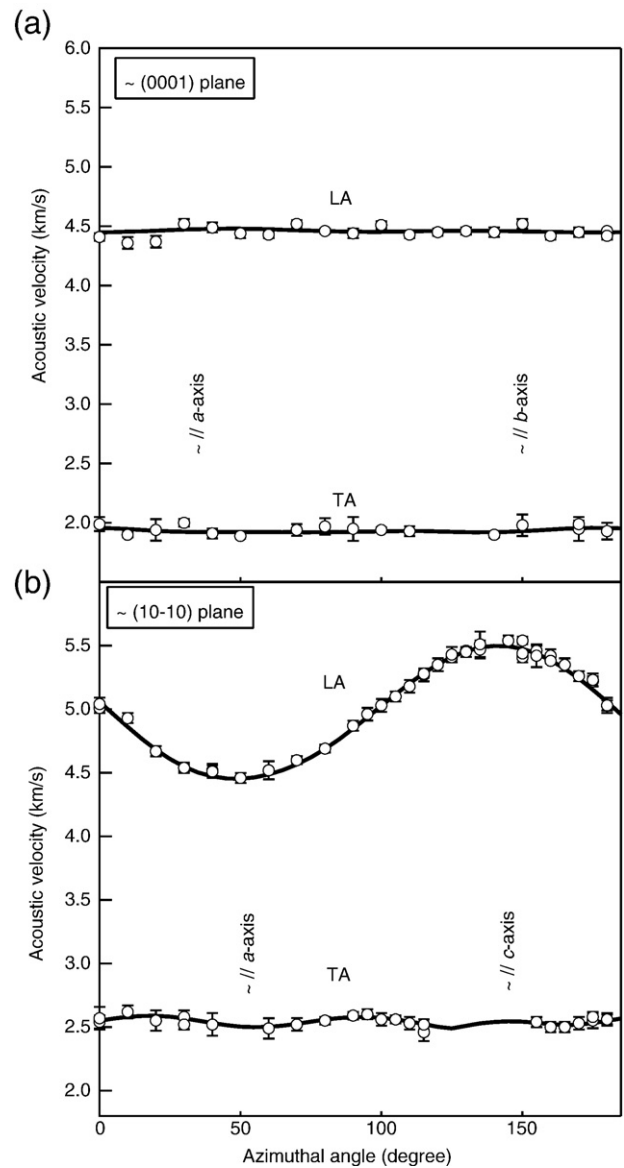


Fig. 3. Spatial dispersion of the quasi-longitudinal and quasi-transverse acoustic velocity in the two crystallographic planes of ettringite. (a) basal plane (-0.1 0.14 - 0.04 1.91). (b) Plane (1 -0.15 -0.85 -0.57). LA: quasi-longitudinal acoustic velocity. TA: quasi-transverse acoustic velocity. Circles: measured velocities. Lines: velocities calculated according to the elastic constants determined in this study (Table 2).

Table 2

Elastic constants of ettringite and Young's modulus in selected directions at ambient conditions

Constant	(GPa)
C_{11}	35.1 ± 0.1
C_{12}	21.9 ± 0.1
C_{13}	20.0 ± 0.5
C_{14}	0.6 ± 0.2
C_{33}	55 ± 1
C_{44}	11.0 ± 0.2
C_{66}^a	6.6 ± 0.1
E_{001}	41 ± 1
E_{100}	20.1 ± 0.3
E_{110}	20.1 ± 0.3

^a C_{66} is calculated as $(C_{11} - C_{12})/2$. E_{hkl} : Young's modulus along the [hkl] crystallographic direction.

A transparent, prismatic fragment, 1-cm long and 0.5-cm wide was picked from a larger crystal. The fragment showed a good prismatic cleavage $\{10\bar{1}0\}$, parallel to the elongation direction. Small fragments of the crystal were observed optically and revealed that the elongation direction was parallel to the *c*-axis (the optic axis). No twinning was observed. We cut and polished 500- μm thick platelets parallel to the elongation direction and a 800- μm thick platelet perpendicular to the elongation direction. Two platelets, one parallel to the *c*-axis and one approximately perpendicular to it, were used for Brillouin spectroscopy measurements. A 150 mW beam of 532.15 nm radiation, produced by a solid state Nd:YVO₄ laser was focused on the crystal platelet. The scattered light was collected and analyzed by a multi-pass tandem Fabry–Perot interferometer [12] and the signal was detected by a photomultiplier tube. The sample platelets were loaded in a 1 cm diameter cylindrical chamber obtained by drilling a hole in a brass plate sandwiched between 500- μm thick glass slides. The sample chamber was filled with mineral oil for thermal dissipation, to prevent sample overheating and dehydration during the experiment.

The experiments were performed in forward symmetric scattering geometry [13]. The angle between the incident and scattered beam outside the glass container was set to 70°. Brillouin scattering was

Table 3

Aggregate elastic moduli of ettringite in comparison with portlandite

Material (study)	Ettringite (this study)	Portlandite H (experim.)	Portlandite L (theor.)
K_R (GPa)	26.90 ± 0.6	32.4	26.6
G_R (GPa)	9.0 ± 0.1	13.4	13.9
E_R (GPa)	24.2 ± 0.3	35.4	35.6
ν_R	0.35 ± 0.01	0.32	0.28
K_V (GPa)	27.7 ± 0.9	46.9	36.2
G_V (GPa)	9.9 ± 0.1	19.3	22.7
E_V (GPa)	26.7 ± 0.3	50.9	56.2
ν_V	0.34 ± 0.01	0.32	0.24
K_H (GPa)	27.3 ± 0.9	39.6	31.4
G_H (GPa)	9.5 ± 0.8	13.4	18.3
E_H (GPa)	25 ± 2	43.1	45.9
ν_H	0.34 ± 0.02	0.32	0.26
K_{HS-} (GPa)	27.15 ± 0.19	37	28.9
G_{HS-} (GPa)	9.40 ± 0.1	14.8	16.5
E_{HS-} (GPa)	25.3 ± 0.3	39.2	41.7
ν_{HS-}	0.34 ± 0.01	0.32	0.26
K_{HS+} (GPa)	27.24 ± 0.20	42.7	32.1
G_{HS+} (GPa)	9.50 ± 0.1	16.9	19.5
E_{HS+} (GPa)	25.5 ± 0.3	44.9	48.7
ν_{HS+}	0.34 ± 0.01	0.32	0.25

H: Holuj et al. (1985) [2]; L: Laugesen (2005) [17].

 K_i : bulk modulus. G_i : shear modulus. E_i : isotropic aggregate Young's modulus. ν_i : isotropic aggregate Poisson's ratio. K_R, G_R, E_R, ν_R : Reuss bounds. K_V, G_V, E_V, ν_V : Voigt bounds. K_H, G_H, E_H, ν_H : Hill averages. $K_{HS-}, G_{HS-}, E_{HS-}, \nu_{HS-}$: Hashin–Shtrikman lower bounds. $K_{HS+}, G_{HS+}, E_{HS+}, \nu_{HS+}$: Hashin–Shtrikman upper bounds.

measured in 36 crystallographic directions in the axial platelet and in 19 directions in the basal platelet. The collection time varied between 5 and 10 min depending on the measured direction.

At selected crystal orientations the measurements were performed in different polarization conditions to enhance the signal to noise ratio. Also some measurements were repeated at different sample positions to test the homogeneity of the sample material. The precision of the frequency shift measurements is better than 0.5% for the quasi-longitudinal mode and better than 3% for the quasi-shear mode. The overall accuracy of the velocity determination was tested on different standard materials at the same experimental conditions and it is better than 1% of the measurement (see also [14]).

3. Results

The spectra collected from both examined crystal platelets show only two spectral features from ettringite, one quasi-longitudinal and one quasi-transverse acoustic mode. The second polarization of the quasi-transverse mode is never visible due to the low elasto-optic coupling in the directions that we examined. Representative spectra for both platelets are presented in Fig. 2. The spatial dispersion of acoustic sound velocity in the two crystallographic planes is plotted in Fig. 3.

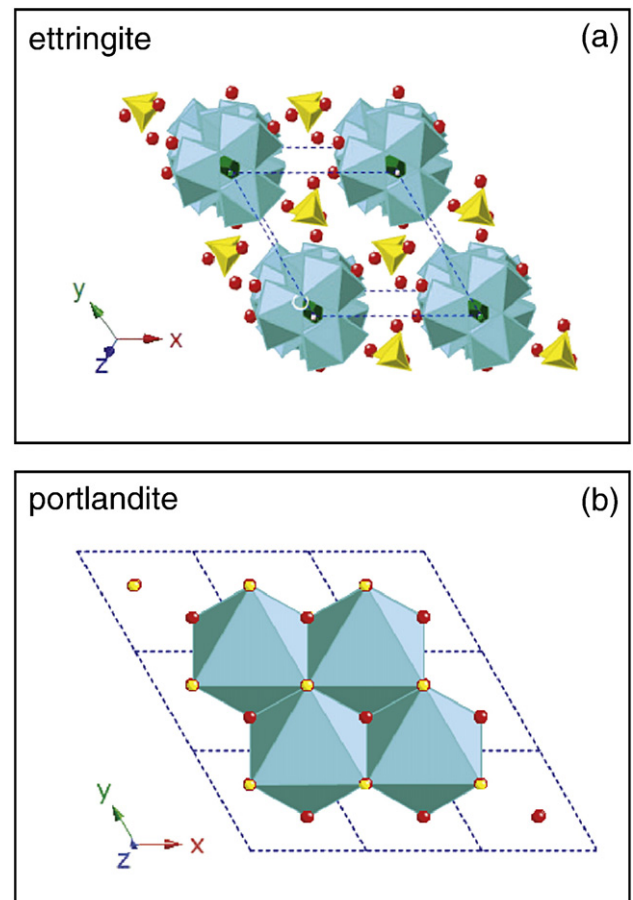


Fig. 4. (a) 3D structural model of ettringite. The most relevant structural unit is represented by columns of $[\text{Al}(\text{OH})_6]^{3-}$ running parallel to the *c*-axis (*z* direction). The $\text{Al}(\text{OH})_6$ octahedra (dark green) in the chains are alternating with Ca^{2+} coordinating eight water molecules (light green polyhedra). Yellow tetrahedra are $[\text{SO}_4]^{2-}$. (b) 3D structural model of portlandite. The structure of portlandite is based on layers of $[\text{Ca}(\text{OH})_6]^{4+}$ octahedra, stacked along the *c*-axis and with the hydrogens in the interlayer. The $[\text{Ca}(\text{OH})_6]^{4+}$ octahedra are drawn in light green, oxygen atoms are represented by red spheres and hydrogens by yellow spheres. (For interpretation of the references to color in this figure legend, the reader is referred to the web version of this article.)

Ettringite crystallizes in the trigonal system (space group $P31c$) and its second order elastic stiffness tensor has 6 independent non-zero components: C_{11} , C_{12} , C_{13} , C_{14} , C_{33} , C_{44} in contracted notation [15]. We determined the acoustic velocity from the measured Brillouin shift and we fit simultaneously all the elastic constants and the orientation of the two measured platelets by inverting, for all the measured acoustic velocities, Christoffel's equation [16]:

$$(C_{iklm}l_k l_m - \rho v^2 \delta_{il})u_l = 0, \quad (1)$$

where C_{iklm} are the elastic constants in full notation, l_k and l_m are the direction cosines of the phonon, u_l is the displacement vector, ρ is the density, v is phonon's velocity, and δ_{il} is the Kronecker delta.

The best fit elastic constants are presented in Table 2. The goodness of the fit is represented by the root-mean-square velocity misfit between calculated and measured velocities that is 0.04 km/s. The orientation of the two platelets was also refined using Eq. (1) and

correspond to $(1\ 0.4\ -0.3)$ and $(-0.1\ 0.1\ 1)$ referred to a standard Cartesian reference system with x_1 coordinate corresponding to the a -crystallographic axis and x_3 corresponding to the c -axis. The orientations of the platelets correspond to $(1\ -0.15\ -0.85\ -0.57\ \sim 10\bar{1}0)$ and $(-0.1\ 0.14\ -0.04\ 1.91\ \sim 0001)$ if referred to a hexagonal reference system (Miller–Bravais indices). The uncertainties on the orientations are better than 4° . The estimated uncertainties on the fit constants are better than 1% for C_{11} and C_{12} , better than 2% for C_{13} , C_{33} , and C_{44} , and as large as 34% for the nearly vanishing C_{14} .

The spatial dispersion of both longitudinal and transverse acoustic velocity is clearly anisotropic (Fig. 3). We can estimate the elastic anisotropy by means of simple ratios of the elastic constants. The ratio $C_{11}/C_{33}=0.64\pm 0.01$ describes the longitudinal elastic anisotropy while the ratio $C_{66}/C_{44}=0.60\pm 0.01$ describes the anisotropy of rigidity between the basal and axial planes. These ratios tell us that the stiffness of ettringite, along the c -axis (along which columns of $[\text{Al}(\text{OH})_6]^{3-}$ polyhedra are aligned) is 40% higher than perpendicular to it, and

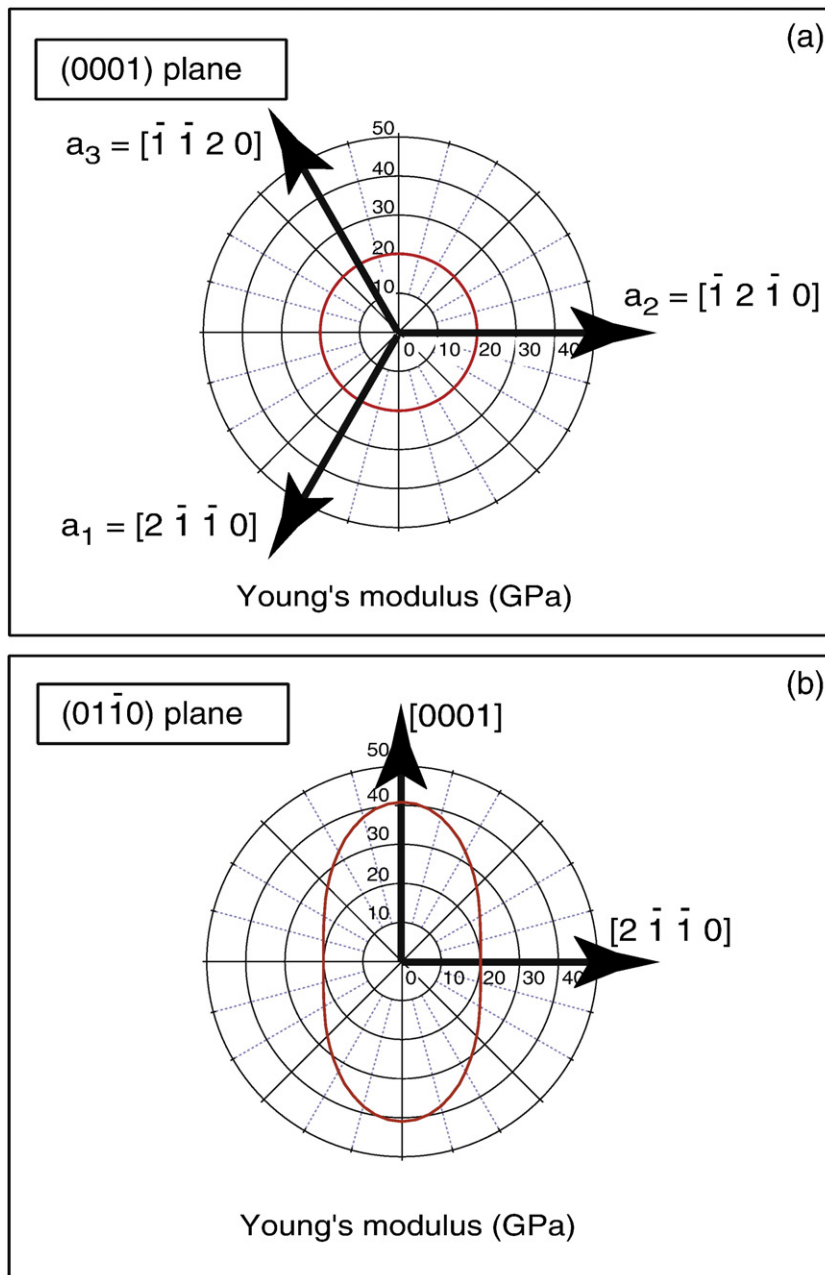


Fig. 5. Polar plot of the Young's modulus along directions in two orthogonal crystallographic planes of ettringite. (a) (0001) plane. (b) $(0\ 1\ -1\ 0)$ plane.

the rigidity within the basal plane is 40% lower than along the *c*-axis (Table 2). The elastic anisotropy of ettringite is substantially different from that of portlandite [$\text{Ca}(\text{OH})_2$] another important component of cement with trigonal symmetry, which is characterized by longitudinal elastic anisotropy $C_{11}/C_{33}=2.9\pm 0.2$ and shear anisotropy $C_{66}/C_{44}=3.8\pm 0.8$ [2,17].

4. Discussion

The Hill average of the Reuss and Voigt bounds [18] for the bulk and shear modulus are $K_{\text{H}}=27.3\pm 0.9$ GPa and $G_{\text{H}}=9.5\pm 0.8$ GPa respectively (Table 3). The tighter Hashin and Shtrikman bounds were also calculated following the method outlined in [19] and they are $K_{\text{HS}^-}=27.15\pm 0.19$ GPa, $G_{\text{HS}^-}=9.4\pm 0.1$ GPa, $K_{\text{HS}^+}=27.24\pm 0.20$ GPa and $G_{\text{HS}^+}=9.5\pm 0.1$ GPa (Table 3). Our results show that ettringite is less stiff than portlandite [2,17] with K_{H} 13% smaller and G_{H} 48% smaller than $\text{Ca}(\text{OH})_2$. The Hill aggregate Young's modulus of ettringite is 25 ± 2 GPa, and it is 45% smaller than portlandite (Table 3).

The elastic tensor of ettringite is strongly anisotropic. The anisotropy is directly related to the main structural features of this mineral. The chains of $[\text{Al}(\text{OH})_6]^{3-}$ octahedra running parallel to the *c*-crystallographic axis (Fig. 4) represent the stiffest structural feature of ettringite and they are responsible for a 50% anisotropy of the Young's modulus between axial and basal directions (Fig. 5).

The pattern of elastic anisotropy of ettringite is substantially different from portlandite, reflecting the very different crystal structure of the two minerals. In fact portlandite is a typical representative of the group of bivalent metal hydroxides (brucite group) that are characterized by a layered structure. The structure of portlandite is composed of layers based on Ca octahedrally coordinated by OH groups, which are stacked along the *c*-axis with the hydrogens in the interlayers (Fig. 4). The weak interactions at the interlayers, cause a pronounced elastic anisotropy with a minimum of Young's modulus along the *c*-axis. The elastic anisotropy is reflected in the crystal shape of portlandite, which is platy, with well developed basal planes.

Both ettringite and portlandite are characterized by extremely low elastic anisotropy (lower than 1% both in compression and in shear) within the basal plane. Comparing the elastic stiffnesses of ettringite and portlandite along directions in the basal plane we find that ettringite is 65% less stiff in compression ($C_{11\text{E}}/C_{11\text{P}}=0.35$, where $C_{ij\text{E}}$ is the elastic stiffness of ettringite and $C_{ij\text{P}}$ is the corresponding stiffness of portlandite), and 81% less stiff in shear within the basal plane ($C_{66\text{E}}/C_{66\text{P}}=0.19$). On the other hand ettringite is 40% stiffer than portlandite if sheared in meridian planes (containing the three-fold symmetry axis), confirming the fundamental difference between the pattern of elastic anisotropy of these two trigonal minerals: ettringite with the *c*-axis as the stiffest direction, and portlandite where the *c*-axis is the least stiff direction.

In ettringite the larger strength of the interactions across the basal face of the unit-cell is also reflected in the prismatic-fibrous crystal habit with development of large prismatic faces and smaller basal faces, while the opposite is true in portlandite, characterized by strong interactions within basal planes and typical platy crystal habit with large basal faces.

5. Conclusions

We have determined the complete elastic tensor of ettringite at ambient conditions by Brillouin scattering. Ettringite is more than 30% less stiff than portlandite. It has ~40% anisotropy both in terms of

compressional and shear moduli. In addition, the elastic anisotropy of ettringite has a pattern with maximum stiffness along the *c*-axis and minimum along directions in the basal plane, reversed with respect to portlandite. Our results will enhance our ability to model the properties of the early stages of cement paste consolidation and of hardened concrete subject to sulfate attack.

Acknowledgments

The research was supported in part by the NSF (062464) and the Carnegie-DOE Alliance Center (CDAC). S.S. has been supported by Miller Institute for Basic Research in Science at the University of California at Berkeley during the initial stages of the project. P.J.M.M. and H.R.W. appreciate support from KAUST.

References

- [1] A. Every, A. McCurdy, Second and Higher Order Elastic Constants, Landolt-Börnstein – Group III Condensed Matter, vol. 29a, Springer-Verlag, 1992, doi:10.1007/b44185.
- [2] F. Holuj, M. Drozdowski, M. Czajkowski, Brillouin spectrum of $\text{Ca}(\text{OH})_2$, Solid State Commun. 56 (1985) 1019–1021.
- [3] C.J. Haecker, E.J. Garboczi, J.W. Bullard, R.B. Bohn, Z. Sun, S.P. Shah, T. Voigt, Modeling the linear elastic properties of Portland cement paste, Cem. Concr. Res. 35 (2005) 1948–1960.
- [4] S.V. Mattigod, D. Rai, L.E. Eary, C.C. Ainsworth, Geochemical factors controlling the mobilization of inorganic constituents from fossil fuel combustion residuals: I. Review of the major elements, J. Environ. Qual. 19 (1990) 187–201.
- [5] R.K. Fowler, S.J. Traina, J.M. Bigham, U.I. Soto, Solution chemistry and mineralogy of clean coal technology by-products in a long term equilibration study, Ag. Abstr. 30 (1993).
- [6] P.K. Mehta, P.J.M. Monteiro, Concrete: Microstructure, Properties and Materials, Third edition McGraw-Hill, 2006.
- [7] C.M. Linklater, Y. Albinsson, W.R. Alexander, I. Casas, I.G. Mckinley, P. Sellin, A natural analogue of high pH cement pore waters from Maqarin area of Northern Jordan: comparison of predicted and observed trace element chemistry of uranium and selenium, J. Cont. Hydrol. 21 (1996) 59–69.
- [8] B. Cairncross, N.J. Beukes, J. Gutzmer, The Manganese Adventure: The South African Manganese Field, 1997 Associated Ore and Metal Corporation, Johannesburg, South Africa.
- [9] S.J. Barnett, C.D. Adam, A.R.W. Jackson, Solid solution between ettringite $\text{Ca}_6\text{Al}_2(\text{SO}_4)_3(\text{OH})_{12}\cdot 26\text{H}_2\text{O}$, and thaumasite $\text{Ca}_3\text{SiSO}_4\text{CO}_3(\text{OH})_6\cdot 12\text{H}_2\text{O}$, J. Mater. Sci. 35 (2000) 4109–4114.
- [10] S.J. Barnett, D.E. MacPhee, E.E. Lachowski, N.J. Crammond, XRD, EDX and IR analysis of solid solutions between thaumasite and ettringite, Cem. Concr. Res. 32 (2002) 719–730.
- [11] F. Goetz-Neunhoeffer, J. Neubauer, Refined ettringite ($\text{Ca}_6\text{Al}_2(\text{OH})_{12}\cdot 26\text{H}_2\text{O}$) structure for quantitative X-ray diffraction analysis, Powder Diff. 21 (2005) 4–11.
- [12] S.M. Lindsay, M.W. Anderson, J.R. Sandercock, Construction and alignment of a high-performance multipass Vernier tandem Fabry-Perot interferometer, Rev. Sci. Instr. 52 (1981) 1478–1486.
- [13] C.H. Withfield, E.M. Brody, W.A. Bassett, Elastic moduli of NaCl by Brillouin scattering at high pressure in a diamond-anvil cell, Rev. Sci. Instr. 47 (1976) 942–947.
- [14] S. Speziale, T.S. Duffy, Single-crystal elastic constants of fluorite (CaF_2) to 9.3 GPa, Phys. Chem. Miner. 29 (2002) 465–472.
- [15] J.F. Nye, Physical Properties of Minerals, Clarendon Press, Oxford, UK, 1985.
- [16] B. Auld, Acoustic Fields and Waves in Solids, Vol. 1, John Wiley and Sons. New York, London, Sidney, Toronto, 1973.
- [17] J.L. Laugesen, Density functional calculations of elastic properties of portlandite, $\text{Ca}(\text{OH})_2$, Cem. Concr. Res. 35 (2005) 199–202.
- [18] J.P. Watt, G.F. Davies, R.J. O'Connell, The elastic properties of composite materials, Rev. Geophys. Space Phys. 14 (1976) 541–563.
- [19] J.P. Watt, L. Peselnik, Clarification of the Hashin–Shtrikman bounds on the effective elastic moduli of polycrystals with hexagonal, trigonal, and tetragonal symmetries, J. Appl. Phys. 51 (1980) 1525–1531.
- [20] A.E. Moore, H.F. Taylor, Crystal structure of ettringite, Acta Crystallogr. B26 (1970) 386–393.
- [21] ICDD, F. McClune (Eds.), Powder Diffraction File, International Centre for Diffraction Data. 12 Campus Blvd, Newton Square, Pennsylvania U.S.A., 1989.
- [22] R. Berliner, The structure of ettringite, Material Science of Concrete Special Volume, The Sidney Diamond Symposium, American Ceramic Society, 1998, pp. 127–141.
- [23] M.R. Hartman, R. Berliner, Investigation of the structure of ettringite by time-of-flight neutron powder diffraction techniques, Cem. Concr. Res. 36 (2006) 364–370.